HHS Public Access

Author manuscript

Science. Author manuscript; available in PMC 2021 April 21.

Published in final edited form as:

Science. 2018 December 07; 362(6419): 1177–1182. doi:10.1126/science.aap7607.

Mutations in LZTR1 drive human disease by dysregulating RAS ubiquitination

M. Steklov[#1,2], **S. Pandolfi**[#1,2], **M. F. Baietti**[#1,2], **A. Batiuk**[1,2], **P. Carai**[3], **P. Najm**[1,2], **M. Zhang**[4], **H. Jang**[4], **F. Renzi**[1,2], **Y. Cai**[1,2], **L. Abbasi Asbagh**[1,2], **T. Pastor**[1,2], **M. De Troyer**[1,2], **M. Simicek**[1,2], **E. Radaelli**[5], **H. Brems**[5], **E. Legius**[5], **J. Tavernier**[6,7], **K. Gevaert**[6,7], **F. Impens**[8], **L. Messiaen**[5,9], **R. Nussinov**[4,10], **S. Heymans**[3,11,12], **S. Eyckerman**[6,7], **A. A. Sabina**[1,2,†]

[1]VIB-KU Leuven Center for Cancer Biology, VIB, 3000 Leuven, Belgium. [2]Department of Oncology, KU Leuven, Herestraat 49, 3000 Leuven, Belgium. [3]Department of Cardiovascular Sciences, Centre for Molecular and Vascular Biology, KU Leuven, Herestraat 49, 3000 Leuven, Belgium. [4]Cancer and Inflammation Program, Leidos Biomedical Research, Inc., Frederick National Laboratory for Cancer Research, National Cancer Institute at Frederick, Frederick, MD 21702, USA. [5]Department of Human Genetics, KU Leuven, Herestraat 49, 3000 Leuven, Belgium. [6]VIB Medical Biotechnology Center, Albert Baertsoenkaai 3, 9000 Ghent, Belgium. [7]Department of Biochemistry, Ghent University, Albert Baertsoenkaai 3, 9000 Ghent, Belgium. [8]VIB Proteomics Core, Albert Baertsoenkaai 3, 9000 Ghent, Belgium. [9]Department of Genetics, University of Alabama, Birmingham, AL 35294, USA. [10]Department of Human Molecular Genetics and Biochemistry, Sackler School of Medicine, Tel Aviv University, Tel Aviv 69978, Israel. [11]Department of Cardiology, CARIM School for Cardiovascular Diseases Faculty of Health, Medicine and Life Sciences, Maastricht University, Netherlands. [12]The Netherlands Heart Institute, Nl-HI, Utrecht, Netherlands.

[#] These authors contributed equally to this work.

Abstract

The leucine zipper–like transcriptional regulator 1 (LZTR1) protein, an adaptor for cullin 3 (CUL3) ubiquitin ligase complex, is implicated in human disease, yet its mechanism of action remains unknown. We found that Lztr1 haploinsufficiency in mice recapitulates Noonan syndrome phenotypes, whereas LZTR1 loss in Schwann cells drives dedifferentiation and proliferation. By trapping LZTR1 complexes from intact mammalian cells, we identified the guanosine

[†]Corresponding author. anna.sablina@kuleuven.vib.be.

Author contributions: M.St., F.R., S.P., and M.Si. performed biochemical experiments; M.St., M.F.B., and S.P. performed cellular experiments; M.F.B. and T.P. performed qRT-PCR analysis; M.F.B. performed PLA analyses; M.F.B. and P.N. performed immunofluorescence experiments; S.P. and M.D.T. performed mice experiments; A.B. and Y.C. generated CRISPR clones; L.A.A. performed experiments on nonimmortalized Schwann cells; E.R. and P.C. performed the immunohistochemistry staining and analysis; S.E., K.G., and J.T. designed and performed the Virotrap screen; F.I. performed the MS analysis; L.M., E.L., and N.R. performed mutation analysis of schwannomatosis patients; R.N., M.Z., and H.J. performed protein simulations; P.C. and S.H. performed the echocardiography analysis; M.St., M.F.B., S.P., and A.A.S. analyzed the data; and A.A.S. wrote the manuscript. All authors discussed the results and commented on the manuscript.

Competing interests: No potential conflict of interest was reported by the authors.

Data and materials availability: We thank the EUCOMM Consortium for providing us Lztr1$^{tm1a\ (EUCOMM)Wtsi}$ embryonic stem cells. Lztr1$^{tm1a(EUCOMM)Wtsi}$ embryonic stem cells are available from EUCOMM under a material transfer agreement with the EUCOMM Consortium.

triphosphatase RAS as a substrate for the LZTR1-CUL3 complex. Ubiquitome analysis showed that loss of Lztr1 abrogated Ras ubiquitination at lysine-170. LZTR1-mediated ubiquitination inhibited RAS signaling by attenuating its association with the membrane. Disease-associated *LZTR1* mutations disrupted either LZTR1-CUL3 complex formation or its interaction with RAS proteins. RAS regulation by LZTR1-mediated ubiquitination provides an explanation for the role of LZTR1 in human disease.

Mutations concurrent with loss of heterozygosity at leucine zipper–like transcriptional regulator 1 (*LZTR1*) are associated with glioblastoma and schwannomatosis (1-3). LZTR1 mutations predispose for pediatric neoplasms and are increased over background in liver and testicular cancers (4, 5). The most recurrent LZTR1 mutation in cancer is an inactivating splice-site mutation at codon 217 (fig. S1) (4, 6). LZTR1 constitutes to Noonan syndrome caused by dysregulation of the guanosine triphosphatase RAS (7-9). However, how LZTR1 contributes to human disease is not known.

To uncover Lztr1 disease mechanisms, we used an Lztr1 deletion mouse model. We found that loss of Lztr1 is lethal between embryonic day 17.5 (E17.5) and birth (fig. S2A). $Lztr1^{+/-}$ male mice exhibited decreased weight (fig. S2, B to D) and facial dysmorphia (Fig. 1A). $Lztr1^{+/-}$ mice, both male and female, displayed heart malformations, including decreased left ventricular systolic function, increased diastolic dimensions, eccentric hypertrophy, increased cardiomyocyte area, and reduced longevity (Fig. 1, B and C, and fig. S2, E and F). Collectively, our results show that $Lztr1^{+/-}$ mice recapitulate some phenotypes of human Noonan syndrome patients, indicating that LZTR1 function is evolutionary conserved.

We engineered several cellular models of LZTR1 loss: mouse embryo fibroblasts (MEFs) derived from $Lztr1^{+/+}$ and $Lztr1^{-/-}$ mouse embryos, primary human Schwann cells expressing short hairpin green fluorescent protein (shGFP) or shLZTR1, and immortalized human Schwann cells and HeLa cells with CRISPR-Cas9–mediated LZTR1-indels (fig. S3). In all tested models, LZTR1 loss increased growth rate (Fig. 1D and fig. S4, A to C). Overexpression of wild-type LZTR1 (wt-LZTR1), but not of LZTR1 mutants, reduced the enhanced growth rate (Fig. 1E and fig. S4, D and E). Loss of LZTR1 in Schwann cells enhanced twodimensional colony and anchorage-independent (AI) growth (Fig. 1F and fig. S4, F to H), and overexpression of wt-LZTR1, but not of disease-associated LZTR1 mutants, suppressed AI growth in LZTR1-indel cells (Fig. 1G). Furthermore, depletion of LZTR1 in Schwann cells showed a gene expression signature (Fig. 1H) resembling that of proliferating Schwann cells during nerve regeneration (10). These data suggest that LZTR1 loss drives Schwann cells from quiescent, myelinating cells into proliferating cells.

LZTR1 acts a substrate adaptor for cullin 3 (CUL3) ubiquitin ligase complexes (11). To identify candidate LZTR1 substrates, we used a mass spectrometry (MS) Virotrap method, which allowed the trapping of protein complexes from intact mammalian cells (fig. S5A) (12). The screen with LZTR1 as bait detected CUL3, Harvey rat sarcoma viral oncogene homolog (HRAS), and neuroblastoma RAS viral oncogene homolog (NRAS) among the top hits (Fig. 2A). The reciprocal Virotrap screen with the HRAS-deltaCAAX mutant, which lacks the last four amino acids, confirmed the complex formation with LZTR1 and identified CUL3 (Fig. 2B). Furthermore, a panRAS antibody that recognizes all RAS isoforms

coimmunoprecipitated with hemagglutinin (HA)–tagged LZTR1. Similarly, Flag-tagged LZTR1 coimmunoprecipitated with endogenous RAS proteins, but not RAC1 (fig. S5B). Moreover, we introduced a Halo-tag HiBiT (13) to the *LZTR1* locus in HeLa cells and MEFs (Fig. 2C and fig. S5, C and D). panRAS antibody coimmunoprecipitated with endogenous RAS and endogenous HiBiT-LZTR1 (Fig. 2C and fig. S5E). Reciprocal coimmunoprecipitations (co-IPs) demonstrated that LZTR1 interacted with each of the three Flag-RAS isoforms (fig. S5F). Together, these results indicate that LZTR1, CUL3, and RAS form a complex.

To test whether the LZTR1-CUL3 complex might control RAS ubiquitination, we performed an in vitro ubiquitination reaction. We observed ubiquitination of wt-HRAS specifically in the presence of the LZTR1-CUL3 complex (fig. S6A). Coexpression of LZTR1 and CUL3 in human embryonic kidney (HEK) 293T cells increased amounts of ubiquitinated RAS (Fig. 2D and fig. S6B). By contrast, treatment with the cullin neddylation inhibitor MLN4924 or loss of LZTR1 led to decreased ubiquitination of all Flag-tagged RAS protein isoforms (fig. S6, C to F). Thus, the LZTR1-CUL3 complex can promote ubiquitination of RAS.

To investigate the role of LZTR1 in ubiquitination of endogenous RAS, we characterized ubiquitination profiles of *Lztr1*$^{+/+}$ and *Lztr1*$^{-/-}$ MEFs by MS (Fig. 2E). Ubiquitome analysis revealed that ubiquitination of Hras at Lys^{170} (K170) was abrogated in MEFs lacking Lztr1 (Fig. 2F and fig. S6G), indicating that endogenous Ras may serve as a substrate for the LZTR1-CUL3 complex. We also optimized a proximity ligation assay (PLA) with paired antibodies to ubiquitin (Ub) and panRAS. Consistent with the MS results, Hras-K170R (Lys^{170}→Arg) knock-in or depletion of LZTR1 led to a decrease in panRAS-Ub proximity signals (Fig. 2G and fig. S7). MS analyses failed to detect any C-terminal peptides of Nras or Kras, perhaps because these isoforms are not highly expressed in MEFs and their C termini are lysine-rich (fig. S8A). However, LZTR1 interacted with (fig. S5F) and ubiquitinated all three RAS isoforms (fig. S6F), consistent with evolutionary conservation of K170 (fig. S8D). Thus, the LZTR1-CUL3 complex appears to mediate ubiquitination of all RAS isoforms.

Although multiple truncating and missense mutations of *LZTR1* have been reported in Noonan syndrome and schwannomatosis (1-3, 14), no recurrent germline *LZTR1* mutations have been identified to date. Additional sequencing analysis of blood samples from schwannomatosis patients revealed several recurrent germline mutations of *LZTR1* within the BTB (broad-complex, tramtrack, and bric-a-brac)–BACK domains predicted to mediate dimerization and CUL3 binding (11, 15) (Fig. 3A). Concordantly, the BTB-BACK LZTR1 mutants, except L812P (Leu^{812}→Pro), exhibited reduced binding to CUL3 (Fig. 3B and fig. S9A). Although LZTR1-L812P retained interaction with CUL3, it failed to form dimers (Fig. 3C). Oligomerization of BTB domains determines the subcellular distribution of CUL3 adaptors (15, 16). Indeed, both endogenous and ectopically expressed HA-tagged LZTR1 showed punctate endomembrane immunostaining (fig. S9B), whereas the BTB-BACK domain LZTR1 mutants, including LTZR1-L812P, showed diffuse cytoplasmic staining (Fig. 3D and fig. S9C).

Missense mutations within the LZTR1 Kelch domain predicted to mediate substrate binding are also found in human disease. In co-IP assays, Kelch domain LZTR1 mutants showed decreased binding to RAS (Fig. 3E). The Kelch domain mutants, like wt-LZTR1, displayed punctate immunostaining, but only wt-LZTR1 led to relocalization of RAS to the LZTR1-CUL3–containing puncta, which represent loci of LZTR1-CUL3–mediated ubiquitination (Fig. 3F and fig. S9, D and E). Consistently, the LZTR1-L812P mutant, which does not form puncta, only weakly ubiquitinated RAS, as did the LZTR1-Y726* (Tyr^{726}→Stop) mutant (Fig. 3G). Thus, disease-associated LZTR1 mutations appear to abrogate RAS ubiquitination by disrupting the formation of the RAS-LZTR1-CUL3 complex.

RAS ubiquitination affects RAS–mitogen-activated protein kinase (MAPK) signaling (17). Loss of LZTR1 led to increased RAS activity and phosphorylation of MEK1/MEK2 and ERK1/ERK2 in all tested model systems, whereas enhanced phosphorylation of V-Akt murine thymoma viral oncogene homolog (AKT) was cell dependent (Fig. 4A and fig. S10). After serum stimulation, $Lztr1^{-/-}$ MEFs showed higher MEK1/MEK2 activity at all time points, whereas $Lztr1^{+/-}$ MEFs had higher MEK1/MEK2 phosphorylation only at later time points (fig. S11A). Thus, Lztr1 abundance may fine-tune the activation of Ras signaling. Restoration of wt-LZTR1 expression in LZTR1-indel cells decreased MEK1/MEK2 activity (fig. S11B). Finally, LZTR1-mutated schwannomas showed strong staining of phosphorylated ERK1/ERK2 compared to wt-LZTR1 nerve trunk (fig. S11, C and D). The MEK1 inhibitor pimasertib abolished the colony growth difference between wt-LZTR1 and LZTR1-mutant cells (fig. S11E). Pimasertib treatment also rescued the embryonic lethality of $Lztr1^{-/-}$ mice (Fig. 4B). Thus, LZTR1-mediated phenotypes arise, at least in part, from increased RAS signaling.

Although our MS analysis detected Ras ubiquitination at several lysines, loss of Lztr1 abrogated ubiquitination of Ras only at K170 (Fig. 4C). Thus, ubiquitination of Hras at K170 may specifically require Lzrt1. Indeed, though LZTR1 depletion hindered ubiquitination of wt-HRAS, it did not affect ubiquitination of the HRAS-K170R mutant (Fig. 4D). Loss of LZTR1 also abolished the difference in Ras ubiquitination between wt-Hras and Hras-K170R MEFs (Fig. 4E and fig. S12A). Nonetheless, the LZTR1-CUL3 complex did ubiquitinate mutant HRAS-K170R in vitro (fig. S6A). The site specificity in vivo could be directed by anchoring of RAS to the membrane. Moreover, overexpression of the HRAS-K170R mutant led to higher activation of ERK1/ERK2 than did overexpression of wt-HRAS, and LZTR1 depletion did not affect ERK1/ERK2 activity in cells overexpressing HRAS-K170R (Fig. 4F and fig. S12B). K170R knock-in MEFs also showed increased MAPK signaling and growth rates (fig. S12, C and D). Collectively, these data indicate that LZTR1-mediated ubiquitination of RAS at K170 suppresses RAS-MAPK signaling.

Ubiquitination of RAS can inhibit its activity by triggering its degradation (18). However, quantitative MS analysis did not reveal an increase in RAS protein abundance in $Lztr1^{-/-}$ MEFs (fig. S6G). wt-LZTR1 and LZTR1-indel Schwann cells treated with the protein synthesis inhibitor cycloheximide also showed similar RAS stability (fig. S12E), Thus, LZTR1 regulates RAS by a nondegradative mechanism. Ubiquitination of RAS also induces its relocalization to endomembranes (19, 20). However, LZTR1 overexpression increased

the endomembrane fraction of both wt-RAS and the HRAS-K170R mutant (fig. S12F). LZTR1 alone also only slightly increased RAS ubiquitination (Fig. 2D) and did not affect the MAPK pathway (fig. S12G), suggesting that LZTR1 overexpression promotes endomembrane localization of RAS independently of its ability to mediate ubiquitination at K170.

To assess how ubiquitination of RAS at K170 controls its activity, we elucidated modes of the interaction between RAS and conjugated Ub. LZTR1 colocalized with NRAS at RAB11–Transferrin receptor–positive recycling endosomes (fig. S13), suggesting that LZTR1 regulates ubiquitination of farnesylated and palmitoylated RAS. Therefore, we performed molecular simulations on lipidated RAS. In the initial structures of Ub conjugated to K170 of RAS, the hypervariable regions (HVRs) of RAS exposed their anchor portions to the solution. The long-lasting simulations showed that Ub secured the anchor portion of the HVR by sequestering the farnesyl and palmitoyl groups (fig. S14). Concordantly to a rapid kinetics of spontaneous insertion of lipidated RAS into the membrane (21-24), the HVRs of nonubiquitinated RAS straightforwardly associated with membranes. However, Ub conjugation to K170 of RAS prevented the HVRs from binding to and inserting into membranes (Fig. 4G). Thus, ubiquitination at K170 may disrupt the association of RAS to the membrane. Indeed, loss of LZTR1 or Hras-K170R knock-in increased the fraction of membrane-bound RAS (Fig. 4, H and I, and fig. S15). These results are all consistent with RAS ubiquitination at K170 inhibiting RAS activity by impairing its association with the membrane.

Our results indicate that LZTR1-mediated ubiquitination of RAS on K170 modulates RAS activity, dysregulation of which leads to human disease. An accompanying study shows that LZTR1 dysregulation also confers drug resistance (25). Understanding this unconventional mechanism of RAS activation may help to identify patients who might benefit from RAS pathway inhibitors and inform new therapeutic approaches for these patients.

Supplementary Material

Refer to Web version on PubMed Central for supplementary material.

ACKNOWLEDGMENTS

We thank R. Sciot for providing us with nerve trunk samples and N. Samyn for technical support in performing Virotrap experiments.

Funding:

H2020 European Research Council (ub-RASDisease) (A.A.S.), Research Foundation Flanders (FWO) fellowships (M.F.B.), FWO Research project G068715N (A.A.S.), and Stichting Tegen Kanker F/2014/257 (A.A.S.); European Research Council FP7 305507 (HOMAGE) (S.H.); FP7-Health-2013-Innovations-1 602156 (HECATOS) (S.H.); the Netherlands Cardiovascular Research Initiative, the Dutch Heart Foundation, CVON2011-ARENA (S.H.), CVON2016-Early HFPEF (S.H.), CVON 2017 (S.H.), ShePREDICTS (S.H.), and CVON2017-ARENA PRIME (S.H.); and federal funds from the Frederick National Laboratory for Cancer Research, NIH, under contract HHSN261200800001E (R.N.), and the Intramural Research Program of the NIH Frederick National Laboratory, Center for Cancer Research (R.N.). The content of this publication does not necessarily reflect the views or policies of the U.S. Department of Health and Human Services nor does mention of trade names, commercial products, or organizations imply endorsement by the U.S. government. All simulations were performed using the high-performance computational facilities of the Biowulf PC/Linux cluster at the National Institutes of Health, Bethesda, MD (https://hpc.nih.gov/).

REFERENCES AND NOTES

1. Paganini I et al., Eur. J. Hum. Genet 23, 963–968 (2015). [PubMed: 25335493]
2. Piotrowski A et al., Nat. Genet 46, 182–187 (2014). [PubMed: 24362817]
3. Smith MJ et al., Neurology 84, 141–147 (2015). [PubMed: 25480913]
4. Cancer Genome Atlas Research Network, Cell 169, 1327–1341. e23 (2017). [PubMed: 28622513]
5. Ge Z et al., Cell Rep. 23, 213–226.e3 (2018). [PubMed: 29617661]
6. Witkiewicz AK et al., Nat. Commun 6, 6744 (2015). [PubMed: 25855536]
7. Chen PC et al., Proc. Natl. Acad. Sci. U.S.A 111, 11473–11478 (2014). [PubMed: 25049390]
8. Johnston JJ et al., Genet. Med 20, 1175–1185 (2018). [PubMed: 29469822]
9. Yamamoto GL et al., J. Med. Genet 52, 413–421 (2015). [PubMed: 25795793]
10. Jessen KR, Mirsky R, J. Anat 200, 367–376 (2002). [PubMed: 12090403]
11. Stogios PJ, Downs GS, Jauhal JJS, Nandra SK, Privé GG, Genome Biol. 6, R82 (2005). [PubMed: 16207353]
12. Eyckerman S et al., Nat. Commun 7, 11416 (2016). [PubMed: 27122307]
13. Schwinn MK et al., ACS Chem. Biol 13, 467–474 (2018). [PubMed: 28892606]
14. Hutter S et al., Acta Neuropathol. 128, 449–452 (2014). [PubMed: 25008767]
15. Genschik P, Sumara I, Lechner E, EMBO J. 32, 2307–2320 (2013). [PubMed: 23912815]
16. Marzahn MR et al., EMBO J. 35, 1254–1275 (2016). [PubMed: 27220849]
17. Nguyen LK, Kolch W, Kholodenko BN, Cell Commun. Signal 11, 52 (2013). [PubMed: 23902637]
18. Zeng T et al., Cell Rep. 7, 871–882 (2014). [PubMed: 24746824]
19. Xu L, Lubkov V, Taylor LJ, Bar-Sagi D, Curr. Biol 20, 1372–1377 (2010). [PubMed: 20655225]
20. Yan H, Jahanshahi M, Horvath EA, Liu HY, Pfleger CM, Curr. Biol 20, 1378–1382 (2010). [PubMed: 20655224]
21. Jang H et al., J. Biol. Chem 290, 9465–9477 (2015). [PubMed: 25713064]
22. Jang H, Banerjee A, Chavan T, Gaponenko V, Nussinov R, J. Biol. Chem 292, 12544–12559 (2017). [PubMed: 28623230]
23. Jang H et al., FASEB J. 30, 1643–1655 (2016). [PubMed: 26718888]
24. Jang H, Muratcioglu S, Gursoy A, Keskin O, Nussinov R, Biochem. J 473, 1719–1732 (2016). [PubMed: 27057007]
25. Bigenzahn JW et al., 362, 1171–1177 (2018).

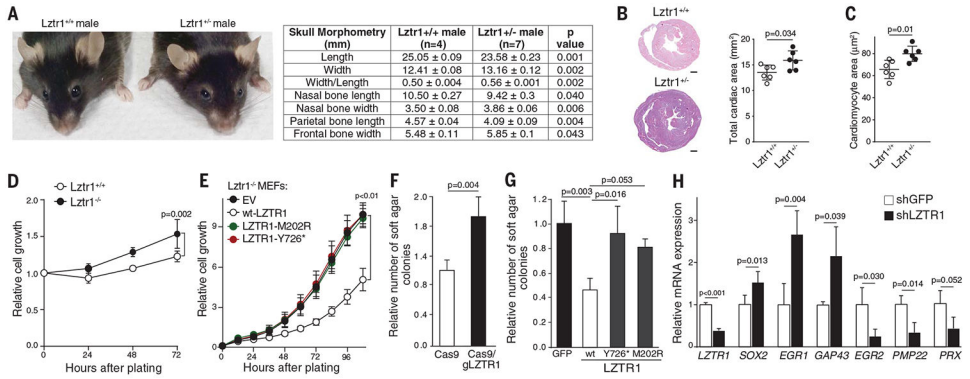

Skull Morphometry (mm)	Lztr1+/+ male (n=4)	Lztr1+/- male (n=7)	p value
Length	25.05 ± 0.09	23.58 ± 0.23	0.001
Width	12.41 ± 0.08	13.16 ± 0.12	0.002
Width/Length	0.50 ± 0.004	0.56 ± 0.001	0.002
Nasal bone length	10.50 ± 0.27	9.42 ± 0.3	0.040
Nasal bone width	3.50 ± 0.08	3.86 ± 0.06	0.006
Parietal bone length	4.57 ± 0.04	4.09 ± 0.09	0.004
Frontal bone width	5.48 ± 0.11	5.85 ± 0.1	0.043

Fig. 1. LZTR1 loss recapitulates disease phenotypes.

(**A**) Morphometric characteristics of the skulls of 12-month-old *Lztr1*$^{+/+}$ and *Lztr1*$^{+/-}$ male mice. (**B**) Haematoxylin and eosin–stained heart ventricular sections. Scale bar, 0.5 mm. The total cardiac area was quantified by Fiji. In the graph, horizontal lines represent means ± SD. (**C**) A mean area of 200 cardiomyocytes measured in laminin-stained heart sections of *Lztr1*$^{+/+}$ and *Lztr1*$^{+/-}$ mice. Horizontal lines represent means ± SD. (**D**) Growth rate of early-passage MEFs isolated from three *Lztr1*$^{+/+}$ and three *Lztr1*$^{-/-}$ embryos. (**E**) Growth rate of *Lztr1*$^{-/-}$ MEFs expressing an empty vector (EV), wt-LZTR1, or LZTR1 mutants. $n = 3$. (**F**) AI growth of Schwann cells expressing Cas9 or Cas9/gLZTR1 (gLZTR1, guide RNA targeting LZTR1). $n = 3$. (**G**) AI growth of LZTR1-indel Schwann cells expressing the indicated constructs. $n = 3$. M202R, Met^{202}→Arg. (**H**) Quantitative real time polymerase chain reaction (qRT-PCR) analysis of mRNA expression in primary human Schwann cells expressing shGFP or pooled shLZTR1. $n = 3$. For (D) to (H), values are means ± SEM. For (A) to (C) and (F) to (H), *P* values are from a two-sided Student's *t* test. For (D) and (E), *P* values were detected by two-way analysis of variance (ANOVA).

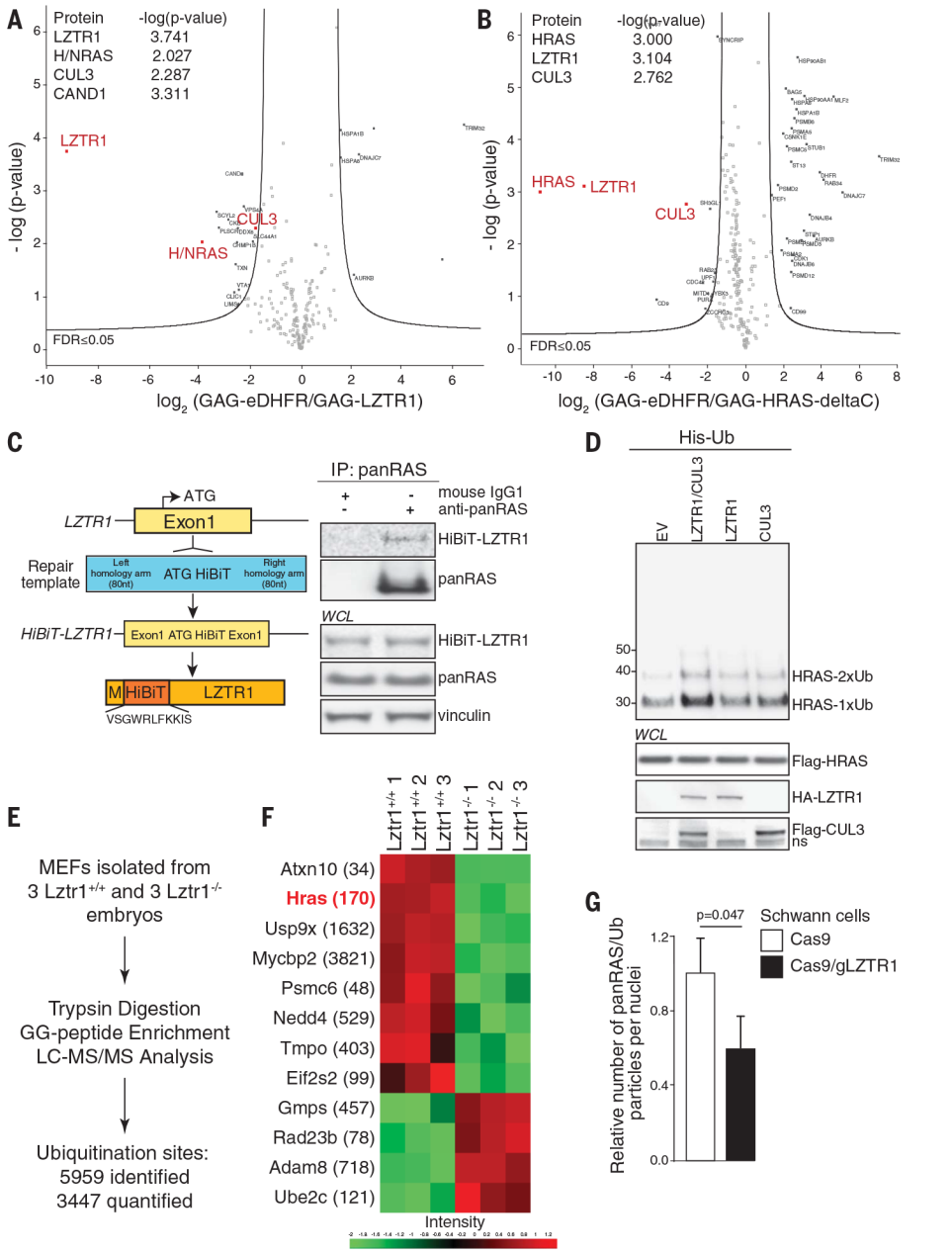

Fig. 2. The LZTR1-CUL3 complex ubiquitinates RAS proteins.

(**A** and **B**) Virotrap screens performed in HEK293T cells using group-specific antigen (GAG)–LZTR1 (A) or GAG-HRAS–deltaCAAX (deltaC) (B) as baits. *Escherichia coli* dihydrofolate reductase (eDHFR) fused to GAG was used as a negative control. (**C**) A scheme for the generation of cells expressing in-frame HiBiT-LZTR1 protein. RAS was immunoprecipitated from the HiBiT-LZTR1 edited HeLa cell lysates with panRAS antibody. Luminescent signal was generated by HiBiT incubated with LgBiT. nt, nucleotide. (**D**) Ubiquitinated RAS was purified from HEK293T cells expressing the indicated constructs by Co^{2+} metal affinity chromatography and detected by immunoblotting. Numbers on the left are molecular masses in kDa. 2xUb, two Ub; 1xUb, one Ub; EV, empty

vector, WCL, whole-cell lysate; ns, nonspecific. (**E**) A workflow for the ubiquitome analysis. LC-MS/MS, liquid chromatography–tandem mass spectrometry. (**F**) A heatmap showing differentially ubiquitinated peptides in *Lztr1*$^{+/+}$ and *Lztr1*$^{-/-}$ MEFs. The scale shows *Z*-scored site intensity values. (**G**) The quantification of the PLA analysis of Schwann cells expressing Cas9 or Cas9/gLZTR1 using antibodies against panRAS and Ub. Values are means ± SEM; $n = 3$. *P* values are from a two-sided Student's *t* test. Single-letter abbreviations for the amino acid residues are as follows: A, Ala; C, Cys; D, Asp; E, Glu; F, Phe; G, Gly; H, His; I, Ile; K, Lys; L, Leu; M, Met; N, Asn; P, Pro; Q, Gln; R, Arg; S, Ser; T, Thr; V, Val; W, Trp; and Y, Tyr.

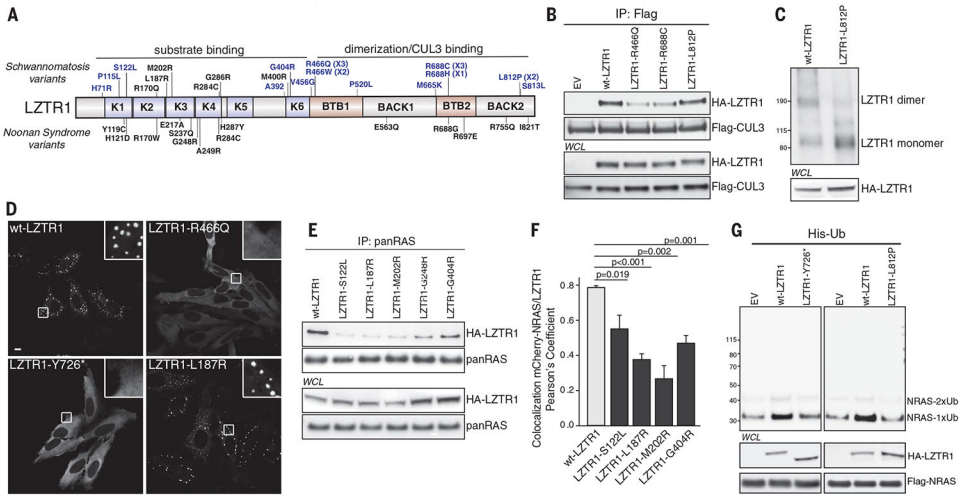

Fig. 3. Disease-associated LZTR1 mutations are loss of function.

(**A**) LZTR1 mutations in schwannomatosis and Noonan syndrome individuals. Missense LZTR1 mutations identified in our cohort of schwannomatosis patients are shown in blue. In the schematic, K indicates Kelch domain. See Fig. 2 legend for amino acid abbreviations. (**B**) Flag-tagged CUL3 purified from HEK293T cells was incubated with HA-tagged LZTR1-overexpressing cell lysates and then immunoprecipitated using anti-Flag resin. LZTR1 was detected by immunoblotting with anti-HA antibody. (**C**) Cross-linking reactions were performed using HA-tagged LZTR1 purified from HEK293T cells. LZTR1 was detected by immunoblotting using anti-HA antibody. (**D**) Immunostaining of HeLa cells expressing HA-tagged wt-LZTR1 or LZTR1 mutants with anti-HA antibody. Scale bar, 10 μm. (**E**) RAS proteins were immunoprecipitated with antibody against panRAS. LZTR1 was detected by immunoblotting with anti-HA antibody. (**F**) Colocalization of mCherry-NRAS and HA-tagged LZTR1 expressed in HeLa-Cas9/gLZTR1 cells. Values are means ± SEM. *P* values were detected by two-sided Student's *t* test. (**G**) Ubiquitinated NRAS was purified from HEK293T cells expressing the indicated constructs by Co^{2+} metal affinity chromatography and detected by anti-Flag antibody.

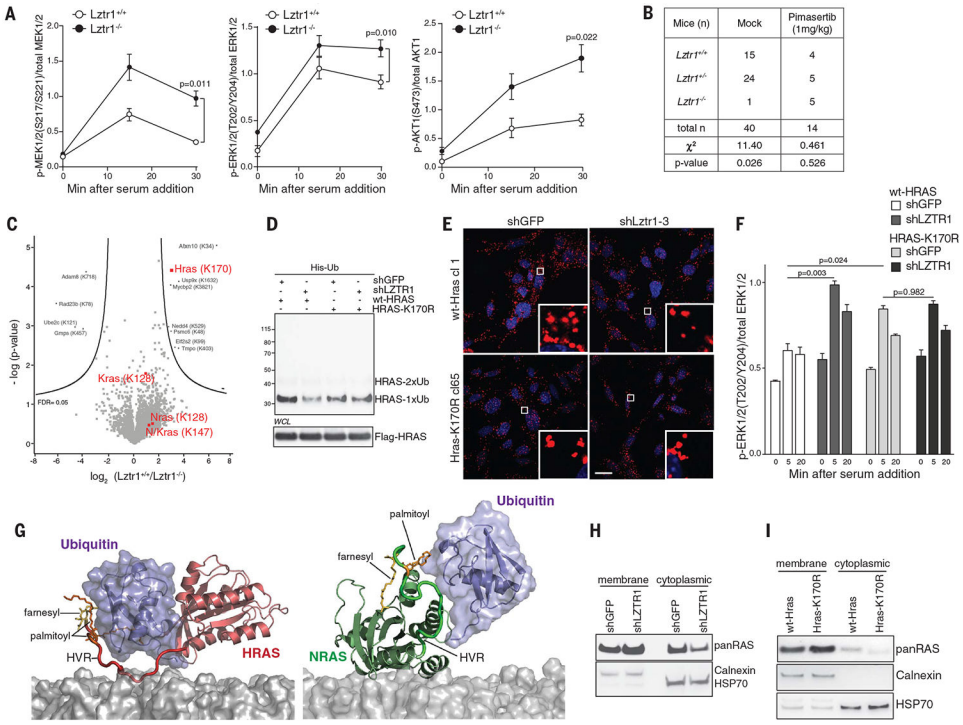

Fig. 4. Ubiquitination at K170 inhibits RAS by impairing its association to the membrane.

(**A**) MEFs isolated from three *Lztr1*$^{+/+}$ and three *Lztr1*$^{-/-}$ embryos were serum-starved, stimulated with 10% serum, and analyzed by immunoblotting. Values are means of phosphorylated (p) relative to nonphosphorylated protein levels ± SEM. *P* values are from a two-way ANOVA. (**B**) Progeny from the indicated *Lztr1*$^{+/-}$ matings. Pregnant mice were treated with pimasertib starting from E7.5. (**C**) Quantitative ubiquitome analysis of *Lztr1*$^{+/+}$ and *Lztr1*$^{-/-}$ MEFs. FDR, false discovery rate. (**D**) Ubiquitinated RAS was purified from HEK293T cells expressing the indicated constructs by Co^{2+} metal affinity chromatography and detected by immunoblotting. (**E**) The PLA analysis of wt-Hras and Hras-K170R MEFs expressing shGFP or shLztr1 using antibodies against panRAS and Ub. Red, PLA signal; blue, 4′,6-diamidino-2-phenylindole; scale bar, 10 μm. (**F**) HEK293T cells expressing the indicated constructs were serum-starved overnight, stimulated with 10% serum, and analyzed by immunoblotting. Values are means of phosphorylated relative to nonphosphorylated protein levels ± SEM; $n = 3$. *P* values are from a two-way ANOVA. (**G**) Snapshots of Ub-conjugated RAS at the lipid bilayer composed of 1,2-dioleoyl-*sn*-glycero-3-phosphocholine (DOPC) and 1,2-dioleoyl-*sn*-glycero-3-phosphoethanolamine (DOPE) lipids (3:1 molar ratio). (**H** and **I**) Immunoblotting of the membrane and cytoplasmic fractions isolated from HeLa cells expressing shGFP and shLZTR1 (H) or wt-Hras and Hras-K170R MEFs (I). HSP70, heat shock protein 70.